Editors' Suggestion

Multiple Tin-Vacancy Centers in Diamond with Nearly Identical Photon Frequency and Linewidth

Yasuyuki Narita,[1] Peng Wang,[1] Keita Ikeda,[1] Kazuki Oba,[1] Yoshiyuki Miyamoto,[2] Takashi Taniguchi,[3] Shinobu Onoda,[4] Mutsuko Hatano,[1] and Takayuki Iwasaki[1,*]

[1] *Department of Electrical and Electronic Engineering, School of Engineering, Tokyo Institute of Technology, Meguro, Tokyo 152-8552, Japan*

[2] *Research Center for Computational Design of Advanced Functional Materials, National Institute of Advanced Industrial Science and Technology, Tsukuba, Ibaraki 305-8568, Japan*

[3] *International Center for Materials Nanoarchitectonics, National Institute for Materials Science, Tsukuba, Ibaraki 305-0044, Japan*

[4] *Takasaki Advanced Radiation Research Institute, National Institutes for Quantum Science and Technology, 1233 Watanuki, Takasaki, Gunma 370-1292, Japan*

(Received 1 October 2022; accepted 18 January 2023; published 23 February 2023)

We report the narrow inhomogeneous distribution of the zero-phonon line from tin-vacancy (Sn-V) centers in diamond and the overlap of spectra from multiple separated Sn-V centers. Photoluminescence excitation spectroscopy measurements at a cryogenic temperature show that Sn-V centers exhibit stable fluorescence and linewidths close to the Fourier-transform-limited linewidth. The inhomogeneous distribution is as low as about 4 GHz, which enables the observation of Sn-isotope-dependent resonant frequencies. Owing to the narrow inhomogeneous distribution, we observe multiple Sn-V centers showing almost identical photon frequencies and linewidths. Identical Sn-V centers are also observed between two diamond samples, confirming the reliable fabrication of high-quality Sn-V centers.

DOI: 10.1103/PhysRevApplied.19.024061

I. INTRODUCTION

Quantum networks require entanglement generation between distant quantum network nodes, including quantum repeaters [1]. Solid-state quantum emitters are a promising platform for quantum light-matter interfaces to construct quantum nodes [2,3]. The generation of quantum entanglement among distant nodes is demonstrated using nitrogen-vacancy (N-V) centers in diamond [4,5], while the N-V center has drawbacks in terms of optical properties: a low fraction of the zero-phonon line (ZPL) against the total emission and a fluorescence line that is subjected to external electric noise. Group-IV color centers in diamond, such as silicon-vacancy (Si-V) [6–8], germanium-vacancy (Ge-V) [9,10], tin-vacancy (Sn-V) [11,12], and lead-vacancy (Pb-V) [13–15] centers, with inversion symmetry, can solve these problems [16–19]. In particular, Sn-V and Pb-V centers are interesting systems from the viewpoint of their spin properties. They are expected to exhibit spin-coherence times of milliseconds at kelvin temperatures, owing to the large spin-orbit interaction in the ground state [11,15]. This is in contrast to the Si-V center, which requires a temperature <1 K in a dilution refrigerator to achieve a long spin-coherence time [20] without a highly strained environment [21]. A spin-coherence time of 0.3 ms is reported for a Sn-V center with all optical operations [22]. Observations of the Fourier-transform-limited linewidth (FTL) [23,24], incorporation in nanocavities [25–27], and two-photon interference using one Sn-V center in nanostructured diamond [28] have also been demonstrated, making the Sn-V center promising as a light-matter interface. However, the generation of photons with identical linewidths and photon frequencies from multiple separated Sn-V centers has yet to be reported; this would play a key role in generating remote entanglement [29] based on the two-photon interference [30,31] between quantum network nodes. Control of the linewidth and wavelength is challenging in solid-state materials, especially for a Sn-V center composed of heavy atoms, because its incorporation into diamond causes more defects and higher strain around the emitters. In this study, we observe Sn-V centers with identical photon frequencies and linewidths formed by ion implantation and subsequent high-temperature annealing at 2100 °C under a high pressure of 7.7 GPa. The Sn-V centers are found to be stable over time and show narrow linewidths close to the FTL. Furthermore, statistical measurements reveal a narrow inhomogeneous distribution, in which we

*iwasaki.t.aj@m.titech.ac.jp

find Sn-isotope-dependent fluorescence energy. Finally, the narrow inhomogeneous distribution enables us to find multiple Sn-V centers with identical photon frequencies and linewidths.

II. EXPERIMENTAL AND CALCULATION METHODS

The Sn-V centers are formed in IIa-type (001) single-crystal diamond substrates (Element Six) by ion implantation and subsequent high-temperature annealing. Ion implantation is performed at an acceleration energy of 18 MeV provided by a 3-MV Tandem accelerator. The mass separator is used to mainly extract $^{120}Sn^{5+}$ ions, and the extracted ion beam passing through the slits after the mass-spectrometry magnet is implanted into the samples with a designed fluence of 5×10^8 cm^{-2}, leading to a projected depth of approximately 3 μm by stopping and range of ions in matter (SRIM) [32]. Then, we conduct a high-temperature treatment for the formation of Sn-V centers [11] at 2100 °C under 7.7 GPa for 20 min using a belt-type high-pressure apparatus [33]. Although surface etching and/or diamond deposition frequently occur during the high-pressure and high-temperature (HPHT) process [15,23], high-energy ion implantation suppresses these effects on the optical properties of the Sn-V centers. We prepare two samples, sample 1 and sample 2, but the surface of sample 2 is polished after the HPHT annealing. Unless otherwise noted, the experimental results are obtained using sample 1. The diamond-surface morphology is observed by optical microscopy (OM) and atomic force microscopy (AFM).

The optical properties are investigated by using a home-built confocal fluorescence microscope equipped with a cryostat (Montana Instruments). All measurements are conducted at a low temperature of about 6 K. A 515-nm green laser (Cobolt Fandango) is used for nonresonant continuous-wave (cw) excitation measurements. The laser is focused onto the sample through a 50× objective lens with a numerical aperture (NA) of 0.95. Fluorescence from the Sn-V centers is directed to avalanche photodiodes or a spectrometer. Photoluminescence excitation (PLE) measurements by resonant excitation are performed by using a dye-tunable laser (Sirah Lasertechnik Matisse 2 DS) at laser powers of 0.8–2.5 nW. A 445-nm repump laser (Cobolt) is also irradiated to measure the stability of the Sn-V emission in Fig. 2(c). The other resonant measurements are conducted only with the resonant laser. A wave meter (Highfinesse WS8-30) with a resolution of 1 MHz is used to monitor the laser wavelength. The phonon sideband (PSB) of the Sn-V centers is detected during resonant excitation. Confocal fluorescence mapping and PLE spectra are recorded with the Qudi program [34]. The excited-state lifetime is measured using a pulsed green laser (PicoQuant D-TA-530B). The signals are recorded with a fast-counting system with a time resolution of 200 ps (FAST ComTec MCS6A).

We estimate vibrational frequencies of the Sn atom in the Sn-V center by first-principles calculations. The frequencies of the Sn atom with A_{2u} (E_u) modes under the ground and excited states are computed from the force field on it by replacing the $\langle 111 \rangle$ ($\langle 1\bar{1}0 \rangle$) crystallographic direction of cubic diamond with an amount of 0.05 bohr. To calculate the force field, density-functional theory (DFT) calculations are performed by using Perdew-Burke-Ernzerhof (PBE) functionals [35], norm-conserving pseudopotentials [36], and conjugate-gradient plane wave schemes, as described in a previous report [37]. Details of the computational conditions are explained in Appendix A. We test the current computational scheme to obtain vibrational energies for Si atoms in the Si-V center and obtain lower values than those reported in previous work [38], which may be due to the choice of the current DFT functional as well as the pseudopotentials being different from the reference values [38].

III. STABILITY OF Sn-V EMISSION

A Sn-V center takes a split-vacancy configuration with an interstitial Sn atom between two carbon vacancies [Fig. 1(a)]. This structure corresponds to D_{3d} symmetry, in which no permanent electric dipole is present. A negatively charged Sn-V center forms the $S = 1/2$ system. The energy levels in the ground and excited states are split due to the spin-orbit interaction, as shown in Fig. 1(b). Thus, four optical transitions (A–D) occur upon nonresonant excitation. Figure 1(c) shows a PL spectrum from ensemble Sn-V

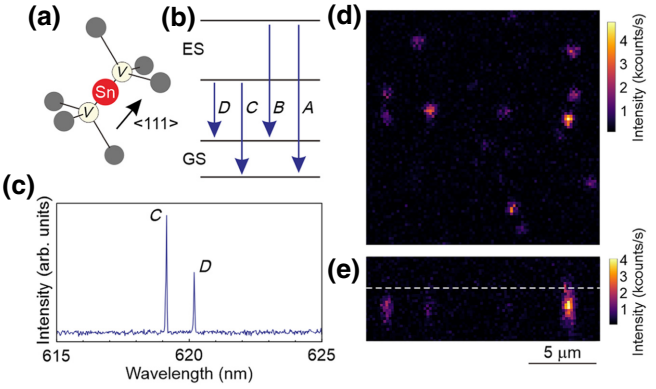

FIG. 1. Structure and optical properties of the Sn-V center. (a) Atomic structure. Main axis is along the $\langle 111 \rangle$ direction. (b) Energy level with a split ground state (GS) and excited state (ES). (c) PL spectrum at about 6 K. Only two lines, called C and D peaks, are observed due to the low electron occupation in the upper level of the excited state at low temperature. (d) Plane and (e) depth confocal scan mappings obtained using a resonant laser on the C peak. Dashed line in (e) indicates the diamond surface, as estimated by laser reflection.

centers at about 6 K. The two sharp lines are the *C* and *D* peaks emitted from the lower level in the excited state to the two ground states. The energy difference corresponding to the ground-state splitting is 821 GHz, in agreement with a previous report [11]. The *A* and *B* peaks are not visible because the thermal energy does not pump electrons to the upper level in the excited state at this temperature. It is worth noting that only one peak can be observed for each of the *C* and *D* peaks, even for the measurement of the ensemble Sn-*V* centers, indicating that the defects created during ion implantation are efficiently recovered by HPHT annealing.

Figure 1(d) shows a confocal plane scan mapping obtained using resonant laser excitation. The PSB is detected during the scan. We see multiple isolated bright spots that are expected to have very close absorption wavelengths. The depth scan in Fig. 1(e) reveals that the bright spots are located at approximately 1.2 μm in depth from the surface, indicated as a dashed line. The correction considering the mismatched refractive index between vacuum and diamond [39] estimates an actual depth of about 3.2 μm (Appendix B). This agrees with the projected depth obtained by the SRIM calculation of the implanted Sn ions.

The stability of the resonant peaks over time is investigated by repeating the scanning of the laser wavelength around the *C* peak at one laser spot. Figure 2(a) shows consecutively measured PLE spectra for a duration of approximately 12 min. Here, we use a low laser power of 0.8 nW to avoid termination of the fluorescence due to charge conversion [23]. At this laser power, fluorescence termination is not observed, even without irradiation from another nonresonant laser, which is utilized for charge recovery [40]. At the measured spot, three bright lines are clearly observed with a frequency separation of about 400 MHz. These lines correspond to different emitters with energy levels slightly modified by the lattice strain. The linewidths of the three peaks are 32, 33, and 32 MHz (from low to high detuning). The excited-state lifetime of the Sn-*V* centers is estimated to be 5.2 ns, corresponding to an FTL of 31 MHz (Fig. 7 in Appendix C). This value is within the previously reported lifetimes of 4–8 ns [11,23,24,28,41]. The statistical measurements of our Sn-*V* centers reveal a mean linewidth of 34 MHz (Fig. 8 in Appendix C), which is close to the FTL. Importantly, the peak positions do not show notable fluctuation, evidencing the very high stability of the Sn-*V* emission, as expected for D_{3d} symmetry with a vanishing permanent electric dipole. The stability of the resonant peak is also examined at another position [Fig. 2(b)]. Again, we see three sharp lines with narrow linewidths: 33 and 32 MHz for the peaks around zero detuning. The two lines even overlap at one confocal spot measurement. This suggests that the inhomogeneous distribution is strongly suppressed in the sample. Note that the gradual increase in the peak intensity of the right peak over time is caused by the drift of the measurement position.

Then, we investigate PLE spectra with a nonresonant repump laser. A high resonant laser power changes the charge state of various color centers, leading to the sudden vanishing of fluorescence [40,42–44]. The application of a repump laser can recover the charge state, and thus, fluorescence, while it may change the charge environment around the emitter and cause spectral diffusion. First, we observe the fluorescence termination of our Sn-*V* center while measuring the PLE spectrum at a higher resonant laser power of 2.5 nW without the repump laser. The measurements are done at a different spot from those in Figs. 2(a) and 2(b). The Sn-*V* center originally taking the −1 charged state is thought to transfer another state [40]. Emission termination continues during the rest of the PLE scan. In contrast, we observe that the addition of the cw 445-nm repump laser (7.7 μW) makes the Sn-*V* center go back to the −1 state after fluorescence termination. The charge transition occurs intermittently during the scan, but the blue repump laser efficiently recovers the charge

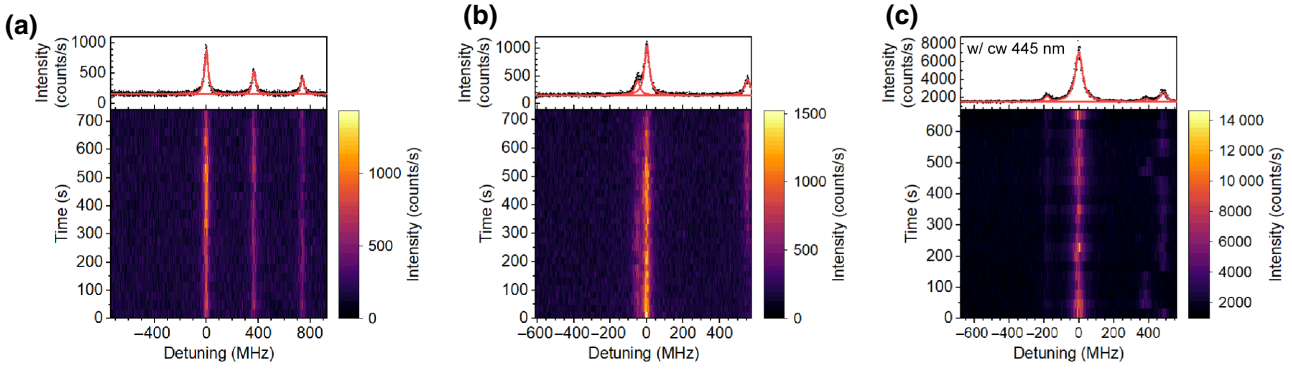

FIG. 2. Stability of the Sn-*V* emission. PLE scans are performed (a),(b) without and (c) with the 445-nm repump laser at different laser spots. For the measurement in (c), a higher resonant power is applied to induce fluorescence termination during the scans. Bottom panels show the stability of the resonant peaks over time. Data in (a)–(c) include 23, 31, and 22 scans, respectively. PLE spectra in the top panels are the averaged curves of the bottom panels. Red curves are fitted.

state [40], enabling the observation of the PLE spectrum. Figure 2(c) shows consecutive scans with the permanently applied 445-nm repump laser. Resonant frequencies of two lines at detunings of 0 and −180 MHz are stable during the scans. In contrast, another peak at 480-MHz detuning shows spectral jumps. The emitter-to-emitter behaviors are caused by the difference in the local charge environment near the emitters [45]. Note that the scheme with pulse irradiation before each scan is expected to mitigate the spectral jump [46] rather than continuous irradiation of the repump laser, which always changes the defect charges. From material and device aspects, the spectral jump is possibly mitigated by further investigations of the formation conditions of the emitters, such as the depth in a bulk crystal [47] and annealing temperature and time, or electrical control of the charge of defects using an electronic device [48].

IV. NARROW INHOMOGENEOUS DISTRIBUTION

The inhomogeneous distribution of the formed Sn-V centers is investigated by performing wide-range PLE scans (47 GHz) at two areas in sample 1, denoted as areas 1 and 2, for a total of 43 spots. Each area is approximately $20 \times 20\ \mu\text{m}^2$ near the center of the sample. Figure 3(a) shows the histogram of the C transition of 160 Sn-V centers. We clearly see three regions in the histogram, hereinafter called P1, P2, and P3. A large portion of Sn-V centers exhibit energy in the P1 region with a narrow FWHM of 3.9 GHz. The three regions are thought to result from the energy shift due to the Sn isotopes. As shown for Si-V and Ge-V centers [10,49–51], the isotope of the group-IV element causes a shift in the ZPL, according to the mass difference. For the preparation of the sample evaluated here, the ion-implantation conditions are set to predominantly select ^{120}Sn ions rather than using the natural abundance. Thus, the P1 regime has the highest count because of the fluorescence from the ^{120}Sn-V centers. However, the other isotopes could be contaminated during ion implantation due to the imperfect isolation of the target ion, resulting from the heaviness of the Sn ions.

Assuming that the local vibration modes of the Sn atom determine the ZPL energy, the energy shift between ^{n}Sn - V and $^{n^*}$Sn - V centers with different masses m_n and m_{n^*} ($m_n < m_{n^*}$) is expressed by [38,49]

$$\Delta E_{n,n^*} = E_n - E_{n^*} = \frac{\hbar}{2}\left(\sum \Omega^e_{n_{S_n}} - \sum \Omega^g_{n_{S_n}}\right) \times \left(1 - \sqrt{\frac{m_n}{m_{n^*}}}\right), \quad (1)$$

where E_n and E_{n^*} are the ZPL energies of the ^{n}Sn - V and $^{n^*}$Sn - V centers, respectively. $\Omega^e_{n_{S_n}}$ and $\Omega^g_{n_{S_n}}$ are the vibration frequencies of ^{n}Sn-V in the excited and ground states, respectively. The phonon frequencies include the Sn vibrations in both the axial (A_{2u}) and transverse (E_u) directions [38]. It is reported that lighter Si and Ge isotopes lead to the shift of the ZPL to higher energies [49,50]. As demonstrated theoretically, this is because the electron is optically excited from a less-localized state to a localized state, leading to an increase in the vibration frequency in the excited state [38,52]. This makes the difference in the vibration frequencies in Eq. (1) positive, resulting in $\Delta E_{n,n^*} > 0$. Our calculations suggest a higher vibration frequency in the excited state than in the ground state for the Sn-V center as well (see Appendix A). Thus, $\Delta E_{n,n^*}$ takes a positive

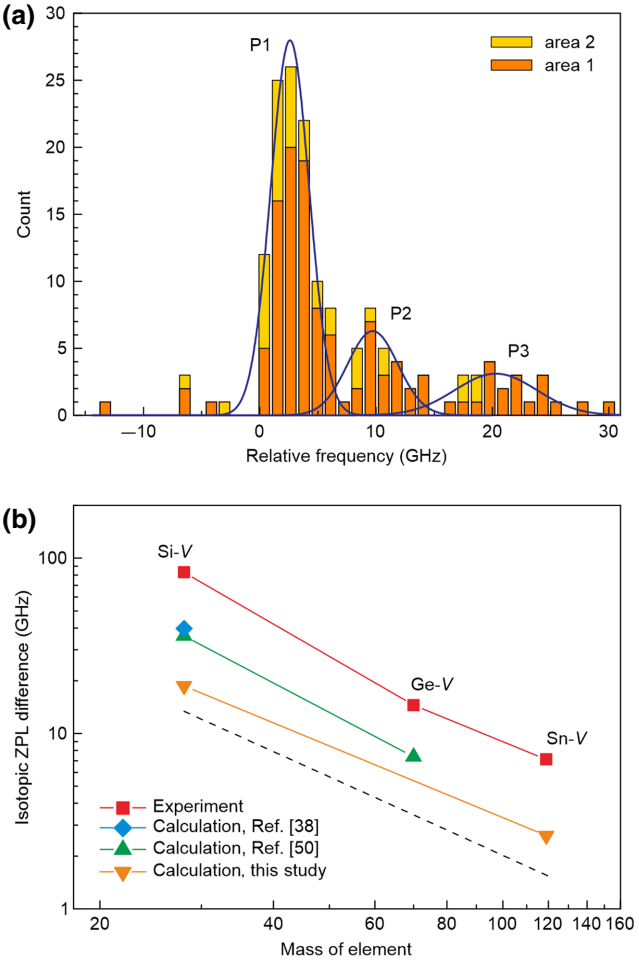

FIG. 3. Inhomogeneous distribution. (a) Histogram of the PLE resonant peaks of 160 Sn-V centers. Measurements are performed in two areas of sample 1, and data are stacked with different colors. Frequency is given as the shift from 484.130 THz. Blue lines are the fitting curves for the three regions. Three peaks of P1, P2, and P3 are thought to correspond to ^{120}Sn-V, ^{119}Sn-V, and ^{118}Sn-V, respectively. (b) Isotopic difference of the ZPL energy depending on the mass of the group-IV element. Experimental values of the Si-V and Ge-V centers are obtained from previous reports [49,50]. Dashed line denotes the relationship $\Delta E_{n,n+1} \propto 1/\sqrt{m_n} - 1/\sqrt{m_{n+1}}$.

value, and accordingly, the Sn-V center composed of the lighter Sn isotope shows a higher photon energy. This means that P2 and P3, with higher energies, are thought to correspond to lighter isotopes, i.e., ^{119}Sn-V and ^{118}Sn-V centers, respectively. From Eq. (1), $\Delta E_{118,119}$ and $\Delta E_{118,120}$ are expressed as

$$\Delta E_{118,119} = \frac{\hbar}{2}\left(\sum \Omega^{e}_{^{118}S_n} - \sum \Omega^{g}_{^{118}S_n}\right)\left(1 - \sqrt{\frac{m_{118}}{m_{119}}}\right), \tag{2}$$

$$\Delta E_{118,120} = \frac{\hbar}{2}\left(\sum \Omega^{e}_{^{118}S_n} - \sum \Omega^{g}_{^{118}S_n}\right)\left(1 - \sqrt{\frac{m_{118}}{m_{120}}}\right). \tag{3}$$

Accordingly, the ratio of the ZPL shift becomes

$$\frac{\Delta E_{118,119}}{\Delta E_{118,120}} = \frac{1 - \sqrt{m_{118}/m_{119}}}{1 - \sqrt{m_{118}/m_{120}}} = 0.5. \tag{4}$$

From the Gaussian fitting of the histogram in Fig. 3(a), $\Delta E_{118,119}$ and $\Delta E_{118,120}$ are estimated to be 10.6 and 17.7 GHz, respectively. These values lead to a ratio of the ZPL shift ($\Delta E_{118,119}/\Delta E_{118,120}$) of about 0.6, which roughly agrees with the theoretical ratio. The natural abundance of the Sn isotopes close to ^{120}Sn is ^{117}Sn : ^{118}Sn : ^{119}Sn : ^{120}Sn : ^{122}Sn = 7.7% : 24.2% : 8.6% : 32.6% : 4.6% [53]. While ^{120}Sn ions are dominantly implanted in this study, ^{119}Sn has a high possibility of contaminating the sample, leading to the P2 region in Fig. 3(a). Although ^{118}Sn is two mass units different from ^{120}Sn, its high natural abundance causes the P3 region. The linewidth of P3 is clearly broader than those of the other two regions; this possibly originates from residual strain in the diamond lattice. This might lead to the discrepancy of the ZPL shift ($\Delta E_{118,119}/\Delta E_{118,120}$) from theory. Note that we observe a few peaks in the higher positive detuning outside of the region in Fig. 3(a) during 10 scans at different spots; these may also appear due to strain. It is worth stressing that the isotope-distinguished observation of ^{119}Sn-V is important for utilizing a long-lived nuclear spin for quantum memory [21,54,55].

Here, we discuss the isotopic energy shift depending on the group-IV element. Experimentally, the energy shifts against the unit isotopic mass change are 87, 15, and 7 GHz for Si-V [49], Ge-V [50], and Sn-V centers (between ^{119}Sn-V and ^{120}Sn-V in this study), respectively. The heavier group-IV emitter shows a smaller isotopic shift. The calculation of the vibration frequencies of the A_{2u} and E_u modes of the group-IV impurity gives rise to the theoretical energy shift using Eq. (1) [38]. The value of the Si-V center estimated by the first-principles calculation [38] is plotted in Fig. 3(b). In this study, we calculated the vibration frequencies of the Si-V and Sn-V centers by first-principles calculations, showing the decrease in the energy shift as a function of the mass of the group-IV elements [Fig. 3(b)]. Another calculation [50] of the Si-V and Ge-V centers shows a similar decreasing tendency. With the relationship of $\Omega_{n_{S_n}} = \sqrt{k/m_n}$, where k is the force constant, the energy shift against the unit isotopic mass change, $\Delta E_{n,n+1}$, becomes proportional to $1/\sqrt{m_n} - 1/\sqrt{m_{n+1}}$, according to Eq. (1). This relationship is shown as the dashed line in Fig. 3(b), the slope of which agrees with the experiment and calculations. Thus, the decreasing tendency would predominantly originate from the group-IV impurity mass with modification of the force constant.

The highest count group (P1 region) shows a narrow inhomogeneous distribution with a FWHM of 3.9 GHz, as shown in Fig. 3(a). In the P1 energy range for area 1, the probability that two random emitters have fluorescence energies within 1 FTL (31 MHz) is estimated to be 1.1%. This is comparable to that of V_{Si} in SiC [56]. As shown in Fig. 3(a), we observe similar narrow inhomogeneous distributions at the two different areas in the sample. Furthermore, another sample (sample 2) also shows a narrow inhomogeneous distribution (Fig. 4). The surface of sample 2 is polished after HPHT annealing. The

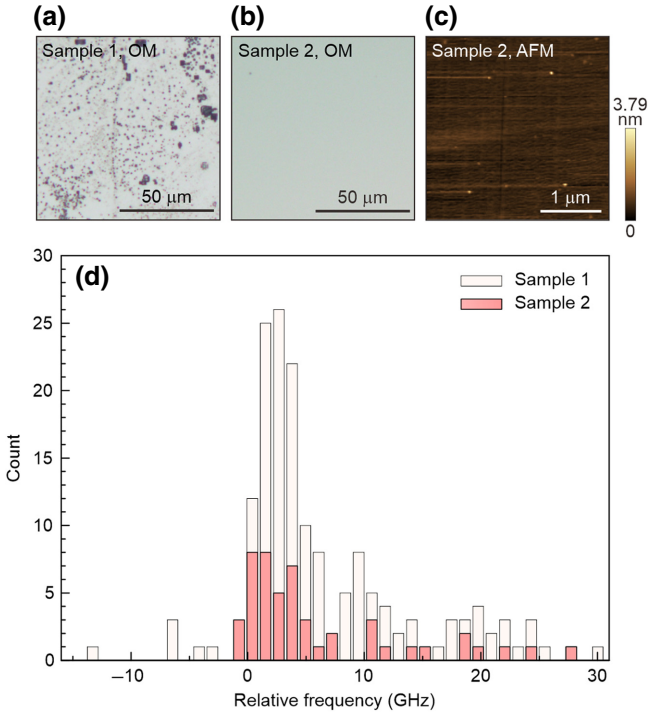

FIG. 4. Inhomogeneous distribution of surface-polished sample (sample 2). OM images of (a) sample 1 and (b) sample 2. (c) AFM image of sample 2. Surface of sample 2 is polished after high-temperature annealing. (d) Histogram of the resonant frequencies of Sn-V centers in sample 2. Histogram of sample 1 is also shown; same data as that in Fig. 3(a). Two sets of data are shown overlaid. Frequency is the shift relative to 484.130 THz.

HPHT annealing process modifies the surface morphology of diamond by etching and/or diamond growth [15], as shown in Fig. 4(a). This hampers the fabrication of nanophotonic structures using high-quality Sn-V centers. To find a solution, here, we test the surface polishing of sample 2. Polishing is done at a miscut angle of 0.5°, and Sn-V centers remaining near the edge of the substrate after polishing are optically measured. As seen in Fig. 4(b), polishing removes the structures formed on the surface. The AFM image in Fig. 4(c) shows a flat surface with a mean roughness of about 0.1 nm, which should be applicable to the fabrication of nanophotonic structures. Figure 4(d) shows the inhomogeneous distribution of the resonant frequencies of 49 Sn-V centers in the polished sample. The resonant frequencies match the three regions observed in sample 1, with the highest count in P1 for sample 2 as well. A Gaussian fitting to the P1 region gives rise to a narrow FWHM of 5.1 GHz. Although this is slightly broader than that of sample 1 (3.9 GHz), it is confirmed that high-quality Sn-V centers are fabricated in another sample.

Within the narrow inhomogeneous distribution, we find Sn-V centers with very close photon frequencies and linewidths. Figure 5(a) shows multiple Sn-V centers with a mutual overlap in the PLE spectra, which is found by performing resonant confocal scanning [7]. In particular, the inner two emitters, about 10 μm apart, show spectra with almost the same linewidths of 35 MHz (green curve) and 38 MHz (blue curve) and a very small energy difference of about 4 MHz, corresponding to about 1/8 FTL. Identical photons at different resonant energies are also shown in Fig. 9 in Appendix D. We investigate sample 2 and find a Sn-V center showing a linewidth of 37 MHz and a resonant energy similar to those in Fig. 5(a). Figure 5(b) depicts the spectral overlap of the emitters in samples 1 and 2. This result further confirms the reliable fabrication of high-quality Sn-V quantum emitters. The generation of identical photons from multiple samples will lead to the observation of two-photon interference between distant Sn-V centers. It is worth noting that, although we do not control the polarization of the fluorescence from the Sn-V centers, it can be adjusted by using polarization optics [7,28,57–59] for two-photon interference.

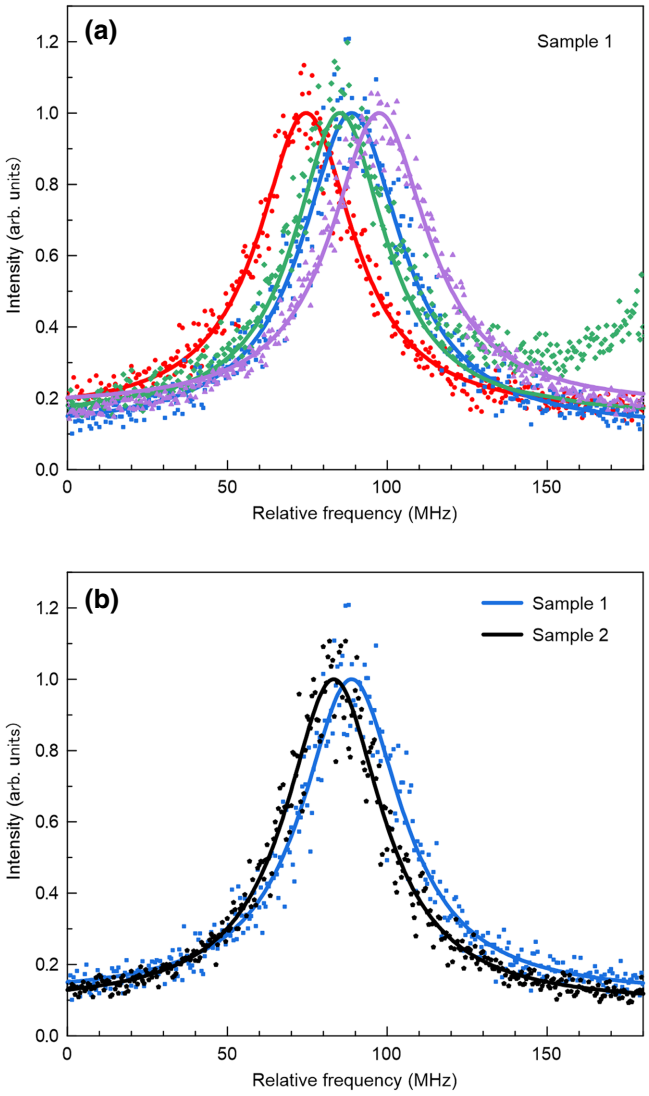

FIG. 5. Observation of multiple Sn-V centers with identical photon frequencies and linewidths. (a) PLE spectra from four Sn-V emitters in sample 1. (b) PLE spectra from two Sn-V emitters in sample 1 and sample 2. Blue spectrum in sample 1 is the same as that in (a). Experimental data are averaged for 3–6 laser scans. Solid lines are fitted. Data and fitting are normalized with the maximum of the fitting for each curve. Frequency is given relative to 484.1319 THz for both panels.

V. DISCUSSION

Among the group-IV color centers in diamond, several studies demonstrate statistically narrow inhomogeneous distributions of Si-V centers. Ion implantation with subsequent annealing shows inhomogeneous distributions of about 15 GHz [60,61]. For Si-V centers in diamond films grown by microwave plasma chemical vapor deposition (CVD) [7,49,62], narrower distributions are observed, with a FWHM of 0.7–8 GHz. Si-V centers in nanodiamonds grown under HPHT also show a narrow distribution of 6.8 GHz [63]. The CVD and HPHT formations lead to the spectral overlap of multiple Si-V centers. This indicates that the direct doping of impurities during diamond growth can reduce strain and defects around the color centers. On the other hand, here, we successfully obtain a narrow inhomogeneous distribution as low as 3.9 GHz, enabling us to observe multiple Sn-V centers with nearly identical photon frequencies formed by ion implantation and subsequent HPHT annealing, even for doping of heavy Sn impurities.

There are two key points in achieving a narrow inhomogeneous distribution of the Sn-V centers based

on ion implantation. One is high-temperature annealing at 2100 °C. Although the heaviness of the Sn ions causes a number of defects in the diamond lattice during ion implantation, high-temperature treatment efficiently addresses lattice damage. Consequently, strain around the emitters is largely suppressed. Another point is ion implantation at a high energy. The Sn-V centers are formed at a depth of about 3 μm from the surface. This suppresses the effect of strain and charged defects at the surface, which potentially shifts the energy level of the emitters. The effect of surface defects on the inhomogeneous distribution will be investigated in the future, e.g., by incorporation into nanostructures [25–27,43,64].

The inhomogeneous distribution of 3.9 GHz obtained in this study is the narrowest among Sn-V centers. Although it is much broader than 1 FTL, the deterministic overlap of multiple Sn-V centers can be achieved with the combination of spectral tuning by strain engineering [65–68] or the Stark shift [69,70]. Strain engineering demonstrates a wide tuning range of over 100 GHz [66], although it requires sophisticated nanofabrication techniques. As another method, voltage application to an emitter alone can control the central frequency by the Stark effect. Its tuning range is thus far limited to about 2 GHz without significant line broadening [69,70], but this will enable us to overlap approximately half of our Sn-V centers in the P1 region (sample 1, area 1) with a narrow inhomogeneous distribution.

VI. CONCLUSION

We fabricate Sn-V centers with a narrow inhomogeneous distribution of photon energy. The Sn-V centers exhibit time-stable resonant energy over 10 min and linewidths close to the FTL. In the histogram of photon energy, three regimes are clearly observed, corresponding to the Sn isotopes. By performing computational calculations, we reveal that a lighter Sn isotope leads to a shift to a higher resonant energy. In the narrowest inhomogeneous distribution region, with a FWHM of 3.9 GHz, we observe multiple Sn-V centers with identical photon energies and linewidths, showing overlapping PLE spectra. The formation of high-quality Sn-V centers directly leads to the observation of two-photon interference between distant emitters and promises further progress of introducing Sn-V centers in diamond to establish a quantum light-matter interface.

ACKNOWLEDGMENTS

This work is supported by JSPS KAKENHI (Grants No. JP22H04962 and No. JP22H00210), the Toray Science Foundation, the MEXT Quantum Leap Flagship Program (Grant No. JPMXS0118067395), and JST Moonshot R&D (Grant No. JPMJMS2062).

APPENDIX A: DETAILS OF THE COMPUTATIONAL SCHEME

The first-principles calculations based on DFT are performed for the Sn-V center in the -1 charged state by using the conjugated-gradient method [37]. The generalized gradient approximation (GGA) for the exchange-correlation potentials, a $3 \times 3 \times 3$ supercell of cubic diamond (216 atoms per cell without vacancies), and Γ point sampling in momentum space are employed. For the GGA, the PBE functional [35] is chosen. Interactions between valence electrons and ions are treated by Troullier-Martins-type pseudopotentials [36]. A cutoff energy of 62 Ry is used for the plane-wave basis set to express the valance-electron wave functions. A spin-unpolarized approximation is used, since the contribution of the spin states is marginal for the force field in the diamond lattice and impurities.

The atomic configuration of the Sn-V center is optimized under the electronic ground and excited states. Both states yield optimized geometries under D_{3d} symmetry. As illustrated in the left panel of Fig. 6, the top-two occupied bands (e_g states) are doubly degenerate and contain three electrons with the -1 charged state. Optical transition matrix elements between the e_g states and the doubly degenerate states just below the valence-band top (e_u states) are recognized as nonzero. This is analogous to the fact reported for the Si-V center [52]. Then, the optically excited state is approximated by promoting one electron from the e_u state to the e_g state, as illustrated in the right panel of Fig. 6.

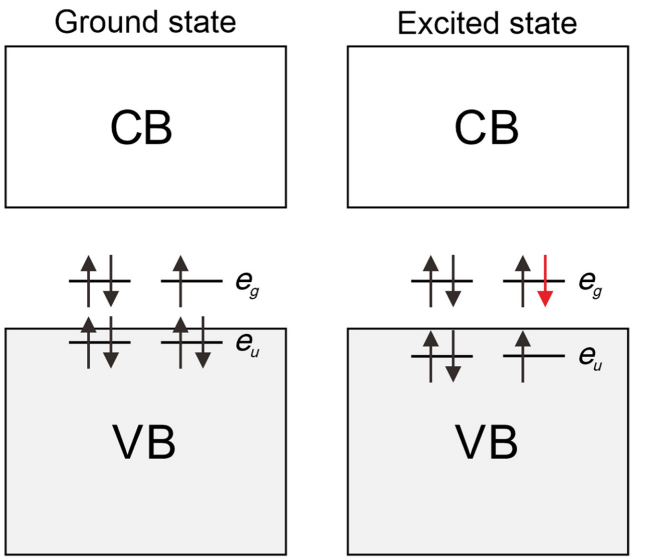

FIG. 6. Energy diagram of the ground and excited states of the Sn-V center with the -1 charged state used for the force-constant calculations. Valence and conduction bands are expressed by shaded and open square boxes, respectively. Red arrow on the right panel shows an optically excited electron. Bars denote energy levels, e_g and e_u states. Note that the e_u level in the right panel is lowered.

TABLE I. Calculated force constants and vibration frequencies for Sn in the Sn-V center.

	Ground state	Excited state
$k_{A_{2u}}$(Hartree/bohr^2)	0.304242	0.381152
k_{E_u}(Hartree/bohr^2)	0.420086	0.435284
$\Omega_{A_{2u}}$(meV)	32.1	35.9
Ω_{E_u}(meV)	37.7	38.4

Within the spin-unpolarized approximation, the ground-state electron occupation is expressed by one electron per spin on the e_u states and by 0.75 electrons per spin on the e_g state. On the other hand, the excited-state electron occupation is expressed by 0.75 electrons per spin on the e_u state and one electron per spin on the e_g state. Contrary to the Si-V case [52], this electron promotion accompanied by geometric optimization further lowers the e_u level, as illustrated in the right panel of Fig. 6.

The zero-point lattice-vibration energy is estimated within the harmonic approximation by taking the A_{2u} mode (Sn replacement in the $\langle 111\rangle$ direction) and doubly degenerate E_u mode (Sn replacement in the $\langle 1\bar{1}0\rangle$ or $\langle \bar{1}10\rangle$ directions) into account. These modes are the same as those of the Si-V center [38]. The ZPL energy of the optical absorption of the Sn-V center is estimated within the harmonic approximation [38,49] as

$$E_{\rm opt}^{\rm gap} + \frac{\hbar}{2}\left[\Omega^e_{^nS_n,A_{2u}} + 2\Omega^e_{^nS_n,E_u} - \Omega^g_{^nS_n,A_{2u}} - 2\Omega^g_{^nS_n,E_u}\right].$$

Here, $E_{\rm opt}^{\rm gap}$ is the optical gap without the phonon contribution, and the second term is the phonon contribution. With the relationship $\Omega_{^nS_n} = \sqrt{k/m_n}$, the energy becomes

$$E_{\rm opt}^{\rm gap} + \frac{\hbar}{2}\frac{1}{\sqrt{m_n}}\left[\sqrt{k^e_{A_{2u}}} + 2\sqrt{k^e_{E_u}} - \sqrt{k^g_{A_{2u}}} - 2\sqrt{k^g_{E_u}}\right],$$

where k and m_n represent the force constant of atomic displacement and mass of a ^{n}Sn atom, respectively. The change in ZPL when ^{n}Sn with a mass of m_n is replaced by $^{n^*}$Sn with a mass of m_{n^*} is given as

$$\Delta E_{n,n^*} = \frac{\hbar}{2}\left(\frac{1}{\sqrt{m_n}} - \frac{1}{\sqrt{m_{n^*}}}\right) \times \left(\sqrt{k^e_{A_{2u}}} + 2\sqrt{k^e_{E_u}} - \sqrt{k^g_{A_{2u}}} - 2\sqrt{k^g_{E_u}}\right).$$

The force field on the Sn atom with the displacement from its stable position by a 0.05-bohr radius is calculated under the electronic excited (ground) state in the $\langle 111\rangle$ direction to obtain the force constants $k^{e(g)}_{A_{2u}}$ and in the $\langle 1\bar{1}0\rangle$ direction to obtain the force constants $k^{e(g)}_{E_u}$. Table I shows the currently computed force constants in these modes under the electronic ground and excited states and the deduced vibration frequencies.

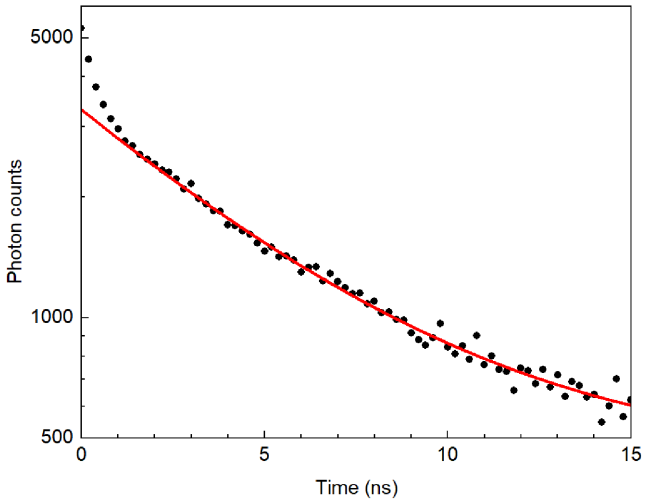

FIG. 7. Estimation of excited-state lifetime.

APPENDIX B: DEPTH OF THE Sn-V CENTER

Experimentally, the depth of the Sn-V is estimated from a confocal fluorescence microscope (CFM) image [Fig. 1(e) in the main text]. The mismatch of the refractive index between diamond and vacuum changes the depth of the CFM image compared to the real depth. Thus, we estimate the real depth of the Sn-V emitter from the CFM image by correcting according to the following relationship [39]:

$$\frac{D}{d} = \frac{\tan(\sin^{-1}(0.5\ {\rm NA}/n_1))}{\tan(\sin^{-1}(0.5\ {\rm NA}/n_2))},$$

where D is the actual laser focus point and d is the distance that the objective lens moves. n_1 and n_2 denote the refractive indices of vacuum (1.0) and diamond (2.4),

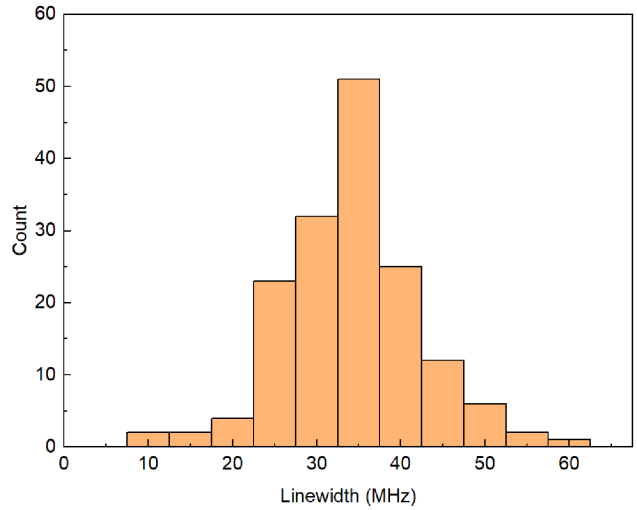

FIG. 8. Distribution of single-scan linewidths of the Sn-V centers (sample 1).

respectively. Using a NA of 0.95, we obtain a correction factor (D/d) of 2.67. Therefore, the observed depth of about 1.2 μm corresponds to an actual emitter depth of about 3.2 μm, which agrees with the estimation by SRIM [32].

APPENDIX C: EXCITED-STATE LIFETIME AND LINEWIDTH DISTRIBUTION

The excited-state lifetime of the Sn-V centers is measured from fluorescence decay after pulse excitations. Figure 7 shows a decay curve with the two decay slopes. The sharp decay between 0 and 1 ns is thought to come from the background emission, including the second-order Raman spectrum of diamond. We fit the curve with a biexponential model. The lifetime of the Sn-V centers is estimated to be $\tau = (5.2 \pm 0.2)$ ns, corresponding to a FTL of (30.6 ± 1.2) MHz.

Figure 8 shows the distribution of single-scan linewidths for the Sn-V centers composing the narrow inhomogeneous distribution in Fig. 3(a). We obtain a mean linewidth of 34 MHz, which is close to the FTL estimated above.

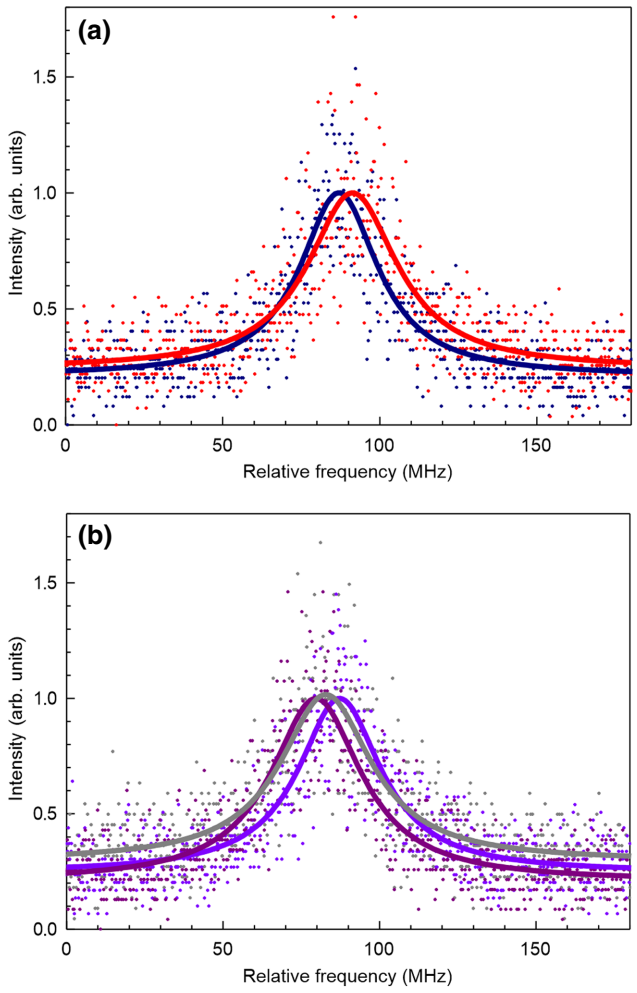

FIG. 9. Sn-V centers with nearly identical photon frequencies and linewidths. Spectral overlap of (a) two and (b) three Sn-V centers. Experimental data are obtained with a single laser scan. Solid lines are fitted. Data and fitting are normalized with the maximum of the fitting for each curve. Frequency is given relative to 484.13 085 THz in (a) and 484.1312 THz in (b).

APPENDIX D: OTHER SETS OF Sn-V CENTERS WITH NEARLY IDENTICAL PHOTON FREQUENCIES AND LINEWIDTHS

Figure 9 shows other measurements of Sn-V centers with almost the same photon frequencies and linewidths at different resonant energies in sample 1. In Fig. 9(a), the two Sn-V centers have linewidths of 30 MHz (blue curve) and 35 MHz (red curve) with a center separation of about 4 MHz. Another measurement in Fig. 9(b) depicts the spectral overlap of three separated Sn-V centers, again with narrow linewidths of 34–37 MHz, showing that most of the peak areas overlap among the three emitters.

[1] H. J. Kimble, The quantum internet, Nature **453**, 1023 (2008).
[2] M. Atatüre, D. Englund, N. Vamivakas, S. Y. Lee, and J. Wrachtrup, Material platforms for spin-based photonic quantum technologies, Nat. Rev. Mater. **3**, 38 (2018).
[3] D. D. Awschalom, R. Hanson, J. Wrachtrup, and B. B. Zhou, Quantum technologies with optically interfaced solid-state spins, Nat. Photonics **12**, 516 (2018).
[4] B. Hensen, H. Bernien, A. E. Dreaú, A. Reiserer, N. Kalb, M. S. Blok, J. Ruitenberg, R. F. L. Vermeulen, R. N. Schouten, C. Abellán, *et al.*, Loophole-free Bell inequality violation using electron spins separated by 1.3 kilometres, Nature **526**, 682 (2015).
[5] M. Pompili, S. L. N. Hermans, S. Baier, H. K. C. Beukers, P. C. Humphreys, R. N. Schouten, R. F. L. Vermeulen, M. J. Tiggelman, L. dos Santos Martins, B. Dirkse, *et al.*, Realization of a multinode quantum network of remote solid-state qubits, Science **372**, 259 (2021).
[6] C. D. Clark, I. J. Thomson, H. Kanda, I. Kiaawi, G. Sittas, and J. J. Thomson, Silicon defects in diamond, Phys. Rev. B **51**, 16681 (1995).
[7] A. Sipahigil, K. D. Jahnke, L. J. Rogers, T. Teraji, J. Isoya, A. S. Zibrov, F. Jelezko, and M. D. Lukin, Indistinguishable Photons from Separated Silicon-Vacancy Centers in Diamond, Phys. Rev. Lett. **113**, 113602 (2014).
[8] C. Hepp, T. Müller, V. Waselowski, J. N. Becker, B. Pingault, H. Sternschulte, D. Steinmüller-Nethl, A. Gali, J. R. Maze, M. Atatüre, *et al.*, Electronic Structure of the Silicon Vacancy Color Center in Diamond, Phys. Rev. Lett. **112**, 036405 (2014).
[9] T. Iwasaki, F. Ishibashi, Y. Miyamoto, Y. Doi, S. Kobayashi, T. Miyazaki, K. Tahara, K. D. Jahnke, L. J. Rogers, B. Naydenov, *et al.*, Germanium-vacancy single color centers in diamond, Sci. Rep. **5**, 12882 (2015).

[10] Y. N. Palyanov, I. N. Kupriyanov, Y. M. Borzdov, and N. V. Surovtsev, Germanium: A new catalyst for diamond synthesis and a new optically active impurity in diamond, Sci. Rep. **5**, 14789 (2015).
[11] T. Iwasaki, Y. Miyamoto, T. Taniguchi, P. Siyushev, M. H. Metsch, F. Jelezko, and M. Hatano, Tin-Vacancy Quantum Emitters in Diamond, Phys. Rev. Lett. **119**, 253601 (2017).
[12] S. D. Tchernij, T. Herzig, J. Forneris, J. Küpper, S. Pezzagna, P. Traina, E. Moreva, I. P. Degiovanni, G. Brida, N. Skukan, *et al.*, Single-photon-emitting optical centers in diamond fabricated upon Sn implantation, ACS Photonics **4**, 2580 (2017).
[13] S. Ditalia Tchernij, T. Lühmann, T. Herzig, J. Küpper, A. Damin, S. Santonocito, M. Signorile, P. Traina, E. Moreva, F. Celegato, *et al.*, Single-photon emitters in lead-implanted single-crystal diamond, ACS Photonics **5**, 4864 (2018).
[14] M. E. Trusheim, N. H. Wan, K. C. Chen, C. J. Ciccarino, J. Flick, R. Sundararaman, G. Malladi, E. Bersin, M. Walsh, B. Lienhard, *et al.*, Lead-related quantum emitters in diamond, Phys. Rev. B **99**, 075430 (2019).
[15] P. Wang, T. Taniguchi, Y. Miyamoto, M. Hatano, and T. Iwasaki, Low-temperature spectroscopic investigation of lead-vacancy centers in diamond fabricated by high-pressure and high-temperature treatment, ACS Photonics **8**, 2947 (2021).
[16] T. Iwasaki, Color centers based on heavy group-IV elements, Semicond. Semimetals **103**, 237 (2020).
[17] M. Ruf, N. H. Wan, H. Choi, D. Englund, and R. Hanson, Quantum networks based on color centers in diamond, J. Appl. Phys. **130**, 070901 (2021).
[18] C. Bradac, W. Gao, J. Forneris, M. E. Trusheim, and I. Aharonovich, Quantum nanophotonics with group IV defects in diamond, Nat. Commun. **10**, 5625 (2019).
[19] D. Chen, N. Zheludev, and W. Gao, Building blocks for quantum network based on group-IV split-vacancy centers in diamond, Adv. Quantum Technol. **3**, 1900069 (2020).
[20] D. D. Sukachev, A. Sipahigil, C. T. Nguyen, M. K. Bhaskar, R. E. Evans, F. Jelezko, and M. D. Lukin, Silicon-Vacancy Spin Qubit in Diamond: A Quantum Memory Exceeding 10 ms with Single-Shot State Readout, Phys. Rev. Lett. **119**, 223602 (2017).
[21] P.-J. Stas, Y. Q. Huan, B. Machielse, E. N. Knall, A. Suleymanzade, B. Pingault, M. Sutula, S. W. Ding, C. M. Knaut, D. R. Assumpcao, *et al.*, Robust multi-qubit quantum network node with integrated error detection, Science **378**, 557 (2022).
[22] R. Debroux, C. P. Michaels, C. M. Purser, N. Wan, M. E. Trusheim, J. Arjona Martínez, R. A. Parker, A. M. Stramma, K. C. Chen, L. De Santis, *et al.*, Quantum Control of the Tin-Vacancy Spin Qubit in Diamond, Phys. Rev. X **11**, 041041 (2021).
[23] J. Görlitz, D. Herrmann, G. Thiering, P. Fuchs, M. Gandil, T. Iwasaki, T. Taniguchi, M. Kieschnick, J. Meijer, M. Hatano, *et al.*, Spectroscopic investigations of negatively charged tin-vacancy centres in diamond, New J. Phys. **22**, 013048 (2020).
[24] M. E. Trusheim, B. Pingault, N. H. Wan, M. Gündoğan, L. De Santis, R. Debroux, D. Gangloff, C. Purser, K. C. Chen, M. Walsh, *et al.*, Transform-Limited Photons from a Coherent Tin-Vacancy Spin in Diamond, Phys. Rev. Lett. **124**, 023602 (2020).
[25] A. E. Rugar, C. Dory, S. Aghaeimeibodi, H. Lu, S. Sun, S. D. Mishra, Z. X. Shen, N. A. Melosh, and J. Vučković, Narrow-linewidth tin-vacancy centers in a diamond waveguide, ACS Photonics **7**, 2356 (2020).
[26] A. E. Rugar, S. Aghaeimeibodi, D. Riedel, C. Dory, H. Lu, P. J. McQuade, Z. X. Shen, N. A. Melosh, and J. Vučković, Quantum Photonic Interface for Tin-Vacancy Centers in Diamond, Phys. Rev. X **11**, 031021 (2021).
[27] K. Kuruma, B. Pingault, C. Chia, D. Renaud, P. Hoffmann, S. Iwamoto, C. Ronning, and M. Lončar, Coupling of a single tin-vacancy center to a photonic crystal cavity in diamond, Appl. Phys. Lett. **118**, 230601 (2021).
[28] J. Arjona Martínez, R. A. Parker, K. C. Chen, C. M. Purser, L. Li, C. P. Michaels, A. M. Stramma, R. Debroux, I. B. Harris, M. Hayhurst Appel, *et al.*, Photonic Indistinguishability of the Tin-Vacancy Center in Nanostructured Diamond, Phys. Rev. Lett. **129**, 173603 (2022).
[29] H. Bernien, B. Hensen, W. Pfaff, G. Koolstra, M. S. Blok, L. Robledo, T. H. Taminiau, M. Markham, D. J. Twitchen, L. Childress, *et al.*, Heralded entanglement between solid-state qubits separated by three metres, Nature **497**, 86 (2013).
[30] C. K. Hong, Z. Y. Ou, and L. Mandel, Measurement of Subpicosecond Time Intervals between Two Photons by Interference, Phys. Rev. Lett. **59**, 2044 (1987).
[31] F. Bouchard, A. Sit, Y. Zhang, R. Fickler, F. M. Miatto, Y. Yao, F. Sciarrino, and E. Karimi, Two-photon interference: The Hong-Ou-Mandel effect, Rep. Prog. Phys. **84**, 012402 (2021).
[32] J. F. Ziegler, M. D. Ziegler, and J. P. Biersack, SRIM - the stopping and range of ions in matter (2010), Nucl. Instrum. Methods Phys. Res., Sect. B **268**, 1818 (2010).
[33] M. Akaishi, H. Kanda, and S. Yamaoka, High pressure synthesis of diamond in the systems of graphite-sulfate and graphite-hydroxide, Jpn. J. Appl. Phys. **29**, L1172 (1990).
[34] J. M. Binder, A. Stark, N. Tomek, J. Scheuer, F. Frank, K. D. Jahnke, C. Müller, S. Schmitt, M. H. Metsch, T. Unden, *et al.*, Qudi: A modular python suite for experiment control and data processing, SoftwareX **6**, 85 (2017).
[35] J. P. Perdew, K. Burke, and M. Ernzerhof, Generalized Gradient Approximation Made Simple, Phys. Rev. Lett. **77**, 3865 (1996).
[36] N. Troullier and J. L. Martins, Efficient pseudopotentials for plane-wave calculations, Phys. Rev. B **43**, 1993 (1991).
[37] M. Saito, A. Oshiyama, and O. Sugino, Energetics and local vibrations of the *DX* center in GaAs, Phys. Rev. B **47**, 13205 (1993).
[38] E. Londero, G. Thiering, L. Razinkovas, A. Gali, and A. Alkauskas, Vibrational modes of negatively charged silicon-vacancy centers in diamond from *ab initio* calculations, Phys. Rev. B **98**, 035306 (2018).
[39] E. E. Diel, J. W. Lichtman, and D. S. Richardson, Tutorial: Avoiding and correcting sample-induced spherical aberration artifacts in 3D fluorescence microscopy, Nat. Protoc. **15**, 2773 (2020).
[40] J. Görlitz, D. Herrmann, P. Fuchs, T. Iwasaki, T. Taniguchi, D. Rogalla, D. Hardeman, P. O. Colard, M. Markham, M.

Hatano, *et al.*, Coherence of a charge stabilised tin-vacancy spin in diamond, npj Quantum Inf. **8**, 45 (2022).

[41] A. E. Rugar, C. Dory, S. Sun, and J. Vučković, Characterization of optical and spin properties of single tin-vacancy centers in diamond nanopillars, Phys. Rev. B **99**, 205417 (2019).

[42] P. Siyushev, H. Pinto, M. Vörös, A. Gali, F. Jelezko, and J. Wrachtrup, Optically Controlled Switching of the Charge State of a Single Nitrogen-Vacancy Center in Diamond at Cryogenic Temperatures, Phys. Rev. Lett. **110**, 167402 (2013).

[43] C. T. Nguyen, D. D. Sukachev, M. K. Bhaskar, B. MacHielse, D. S. Levonian, E. N. Knall, P. Stroganov, C. Chia, M. J. Burek, R. Riedinger, *et al.*, An integrated nanophotonic quantum register based on silicon-vacancy spins in diamond, Phys. Rev. B **100**, 165428 (2019).

[44] D. Chen, Z. Mu, Y. Zhou, J. E. Fröch, A. Rasmit, C. Diederichs, N. Zheludev, I. Aharonovich, and W. B. Gao, Optical Gating of Resonance Fluorescence from a Single Germanium Vacancy Color Center in Diamond, Phys. Rev. Lett. **123**, 33602 (2019).

[45] L. Robledo, H. Bernien, I. Van Weperen, and R. Hanson, Control and Coherence of the Optical Transition of Single Nitrogen Vacancy Centers in Diamond, Phys. Rev. Lett. **105**, 177403 (2010).

[46] L. Orphal-Kobin, K. Unterguggenberger, T. Pregnolato, N. Kemf, M. Matalla, R.-S. Unger, I. Ostermay, G. Pieplow, and T. Schröder, Optically coherent nitrogen-vacancy defect centers in diamond nanostructures, ArXiv:2203.05605 (2022).

[47] B. A. McCullian, H. F. H. Cheung, H. Y. Chen, and G. D. Fuchs, Quantifying the Spectral Diffusion of N-V Centers by Symmetry, Phys. Rev. Appl. **18**, 064011 (2022).

[48] C. P. Anderson, A. Bourassa, K. C. Miao, G. Wolfowicz, P. J. Mintun, A. L. Crook, H. Abe, J. U. Hassan, N. T. Son, T. Ohshima, *et al.*, Electrical and optical control of single spins integrated in scalable semiconductor devices, Science **366**, 1225 (2019).

[49] A. Dietrich, K. D. Jahnke, J. M. Binder, T. Teraji, J. Isoya, L. J. Rogers, and F. Jelezko, Isotopically varying spectral features of silicon-vacancy in diamond, New J. Phys. **16**, 113019 (2014).

[50] E. A. Ekimov, V. S. Krivobok, S. G. Lyapin, P. S. Sherin, V. A. Gavva, and M. V. Kondrin, Anharmonicity effects in impurity-vacancy centers in diamond revealed by isotopic shifts and optical measurements, Phys. Rev. B **95**, 094113 (2017).

[51] E. A. Ekimov, S. G. Lyapin, K. N. Boldyrev, M. V. Kondrin, R. Khmelnitskiy, V. A. Gavva, T. V. Kotereva, and M. N. Popova, Germanium–vacancy color center in isotopically enriched diamonds synthesized at high pressures, JETP Lett. **102**, 701 (2015).

[52] A. Gali and J. R. Maze, *Ab initio* study of the split silicon-vacancy defect in diamond: Electronic structure and related properties, Phys. Rev. B **88**, 235205 (2013).

[53] NIST, *Atomic Weights and Isotopic Compositions for All Elements*, https://physics.nist.gov/cgi-bin/Compositions/stand_alone.pl?ele=&all=all&ascii=html&isotype=some

[54] L. J. Rogers, K. D. Jahnke, M. H. Metsch, A. Sipahigil, J. M. Binder, T. Teraji, H. Sumiya, J. Isoya, M. D. Lukin, P. Hemmer, *et al.*, All-Optical Initialization, Readout, and Coherent Preparation of Single Silicon-Vacancy Spins in Diamond, Phys. Rev. Lett. **113**, 263602 (2014).

[55] M. H. Abobeih, J. Cramer, M. A. Bakker, N. Kalb, M. Markham, D. J. Twitchen, and T. H. Taminiau, One-second coherence for a single electron spin coupled to a multi-qubit nuclear-spin environment, Nat. Commun. **9**, 2552 (2018).

[56] R. Nagy, D. B. R. Dasari, C. Babin, D. Liu, V. Vorobyov, M. Niethammer, M. Widmann, T. Linkewitz, I. Gediz, R. Stöhr, *et al.*, Narrow inhomogeneous distribution of spin-active emitters in silicon carbide, Appl. Phys. Lett. **118**, 144003 (2021).

[57] H. Bernien, L. Childress, L. Robledo, M. Markham, D. Twitchen, and R. Hanson, Two-Photon Quantum Interference from Separate Nitrogen Vacancy Centers in Diamond, Phys. Rev. Lett. **108**, 043604 (2012).

[58] A. Sipahigil, M. L. Goldman, E. Togan, Y. Chu, M. Markham, D. J. Twitchen, A. S. Zibrov, A. Kubanek, and M. D. Lukin, Quantum Interference of Single Photons from Remote Nitrogen-Vacancy Centers in Diamond, Phys. Rev. Lett. **108**, 143601 (2012).

[59] D. Chen, J. E. Fröch, S. Ru, H. Cai, N. Wang, G. Adamo, J. Scott, F. Li, N. Zheludev, I. Aharonovich, *et al.*, Quantum interference of resonance fluorescence from germanium-vacancy color centers in diamond, Nano Lett. **22**, 6306 (2022).

[60] R. E. Evans, A. Sipahigil, D. D. Sukachev, A. S. Zibrov, and M. D. Lukin, Narrow-Linewidth Homogeneous Optical Emitters in Diamond Nanostructures via Silicon Ion Implantation, Phys. Rev. Appl. **5**, 044010 (2016).

[61] J. Lang, S. Häußler, J. Fuhrmann, R. Waltrich, S. Laddha, J. Scharpf, A. Kubanek, B. Naydenov, and F. Jelezko, Long optical coherence times of shallow-implanted, negatively charged silicon vacancy centers in diamond, Appl. Phys. Lett. **116**, 064001 (2020).

[62] L. J. Rogers, K. D. Jahnke, T. Teraji, L. Marseglia, C. Müller, B. Naydenov, H. Schauffert, C. Kranz, J. Isoya, L. P. McGuinness, *et al.*, Multiple intrinsically identical single-photon emitters in the solid state, Nat. Commun. **5**, 4739 (2014).

[63] S. Haußler, L. Hartung, K. G. Fehler, L. Antoniuk, L. F. Kulikova, V. A. Davydov, V. N. Agafonov, F. Jelezko, and A. Kubanek, Preparing single SiV-center in nanodiamonds for external, optical coupling with access to all degrees of freedom, New J. Phys. **21**, 103047 (2019).

[64] T. M. Babinec, B. J. M. Hausmann, M. Khan, Y. Zhang, J. R. Maze, P. R. Hemmer, and M. Lončar, A Diamond nanowire single-photon source, Nat. Nanotechnol. **5**, 195 (2010).

[65] Y. I. Sohn, S. Meesala, B. Pingault, H. A. Atikian, J. Holzgrafe, M. Gündoğan, C. Stavrakas, M. J. Stanley, A. Sipahigil, J. Choi, *et al.*, Controlling the coherence of a diamond spin qubit through its strain environment, Nat. Commun. **9**, 2012 (2018).

[66] S. Meesala, Y. I. Sohn, B. Pingault, L. Shao, H. A. Atikian, J. Holzgrafe, M. Gündoğan, C. Stavrakas, A. Sipahigil, C. Chia, *et al.*, Strain engineering of the silicon-vacancy center in diamond, Phys. Rev. B **97**, 205444 (2018).

[67] S. Maity, L. Shao, Y. I. Sohn, S. Meesala, B. Machielse, E. Bielejec, M. Markham, and M. Lončar, Spectral Alignment

of Single-Photon Emitters in Diamond Using Strain Gradient, Phys. Rev. Appl. **10**, 024050 (2018).

[68] N. H. Wan, T. J. Lu, K. C. Chen, M. P. Walsh, M. E. Trusheim, L. De Santis, E. A. Bersin, I. B. Harris, S. L. Mouradian, I. R. Christen, *et al.*, Large-scale integration of artificial atoms in hybrid photonic circuits, Nature **583**, 226 (2020).

[69] S. Aghaeimeibodi, D. Riedel, A. E. Rugar, C. Dory, and J. Vučković, Electrical Tuning of Tin-Vacancy Centers in Diamond, Phys. Rev. Appl. **15**, 064010 (2021).

[70] L. De Santis, M. E. Trusheim, K. C. Chen, and D. R. Englund, Investigation of the Stark Effect on a Centrosymmetric Quantum Emitter in Diamond, Phys. Rev. Lett. **127**, 147402 (2021).